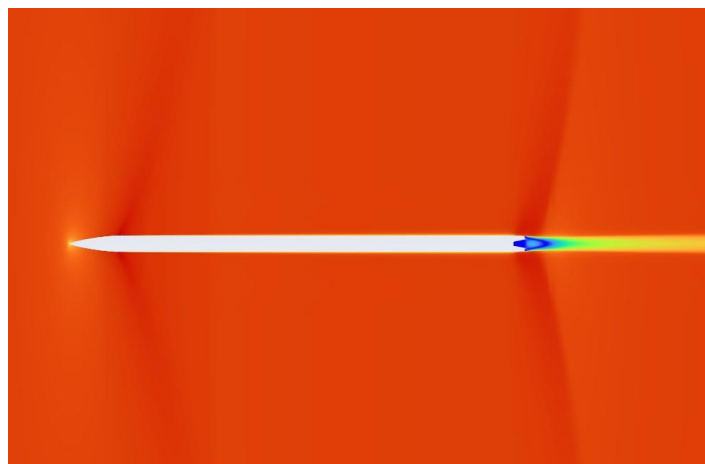Degree Project in Technology

First Cycle, 15 credits

Finding an Empirical Model for a Rocket's Drag Coefficients

A Comparative Analysis with OpenRocket

MAXIMILLIAN SEIZ DE FILIPPI

Abstract

The accuracy of the calculated drag force in *OpenRocket* was examined in this investigation for a rocket traveling at subsonic, transonic and supersonic speeds. The idea was to compare the computed drag coefficients in *OpenRocket* to the drag coefficients obtained by running multiple computational fluid dynamics (CFD) simulations in *Ansys Fluent*. Specifically, the freestream Mach number and altitude parameters were varied for a geometric model of the *Mjöllnir* rocket. The results obtained converged several orders of magnitude and were exceptionally stable. Both the physical accuracy and numerical independence of the results was verified through examining the solutions' contour plots and conducting multiple sensitivity analyses. The conclusion was that *OpenRocket* overpredicts the *Mjöllnir* rocket's drag coefficients by 12% to 73% for all examined freestream Mach numbers and altitudes. Additionally, an empirical relationship was found for how the *Mjöllnir* rocket's drag coefficient changes with altitude and the freestream Mach number. In particular, it is a multivariate function that can be considered valid for an altitude of $h \leq 10\,\mathrm{km}$ and a freestream Mach number of $0.2 \leq M_\infty \leq 3.0$. The empirical relationship fitted exceedingly well with simulation data and merits further investigation.

Acknowledgements

Table of Contents

1   Introduction

1.1   Background

A significant portion of rocket modeling relies on simplified, semi-empirical models that may not always accurately portray reality. This is particularly the case for modeling the aerodynamics of high-power rockets, since most aerodynamic phenomena require either significant computational resources or experimental data to accurately resolve. However, obtaining such data is often prohibitively time-consuming, making it unsuitable for most real-time flight simulations, where quick estimates are necessary. Thereby, developing a significantly more accurate model, that can readily be extended upon and is suitable for real-time simulations, would be of great interest in the field of rocketry.

1.2   Objectives and Goals

The main focus of this research was to determine whether one could accurately approximate the drag coefficient of a three-dimensional rigid-body rocket, when multiple important aerodynamic parameters were varied. This was achieved by computing the drag force experienced by a rocket for specific input values using computational fluid dynamics (CFD) and regression analysis to estimate the drag coefficients for intermediate parameter values. The resulting model could potentially be valid for other similar rocket geometries and be used in real-time applications. Moreover, for real-time applications, this model would primarily only be limited by the range of high-fidelity results that had already been pre-computed. The proposed investigation can be summarized by the following research question:

How accurate are the estimated drag coefficients of a conventional rocket simulator and is the drag coefficient more accurately modeled using data points extracted from CFD software combined with multivariate regression techniques?

1.3   Methods of Investigation

This research was conducted by running multiple CFD simulations in *Ansys Fluent*, where each simulation run had different parameter values. These parameters included the freestream Mach number and the atmospheric conditions at different altitudes. Each simulation yielded a data point for the drag force acting on the *Mjöllnir* rocket and the resulting dataset was used to find an empirical model for the rocket's drag coefficients using regression analysis. Finally, the model developed in this paper was evaluated and compared with the aerodynamic model developed by Niskanen (pp. 14-52) for *OpenRocket*, where differences in the models' predictions were discussed and explained.

1.4   Literature Review

Studies conducted in validating standard aerodynamic models for rockets using CFD, such as Hammargren (pp. 31-37) and Sahbon et al. (pp. 37-42), have often concluded that such models are prone to produce unrealistic results for certain inputs. This could potentially be attributed to such models having a tendency of either underfitting or overfitting the dependencies of aerodynamic coefficients to available data. Likewise, determining the aerodynamic coefficients and their dependence

on various input parameters can be a time-consuming process if it is performed for every rocket model constructed. To try to address this problem, Niskanen (pp. 14-52) developed a method to estimate these aerodynamic coefficients by using information of the exact rocket geometry, which was largely based on the work of Hoerner (pp. 16_1-18_26), Fleeman (pp. 22) and Barrowman (pp. 2-92). However, it is difficult to extend the valid range of this model as a result of its many explicit and prohibitive assumptions. Thus, the main aim of this research is to explore the accuracy of the calculated drag coefficients in *OpenRocket* and determine if an alternative approach to modeling a rocket's drag coefficients could yield a more accurate estimation with a greater valid range.

2 Theoretical Considerations

The underlying theory describing the fluid flow and aerodynamic forces experienced by objects traveling at high speeds is briefly outlined in this section. The purpose of this is to clarify the expected results as well as the assumptions made in this investigation. A more extensive review of the theoretical background is provided in Çengel and Cimbala.

2.1 Flow Behavior

The Mach number and Reynolds number are fundamental parameters used to characterize the nature of the flow around rockets traveling at various speeds relative to the surrounding air. Specifically, the Reynolds number can be interpreted as a ratio of inertial forces to viscous forces (Çengel and Cimbala, pp. 310). It is defined as

$$Re = \frac{\rho u L}{\mu_{\mathrm{d}}}, \tag{1}$$

where ρ is the fluid density, L is the characteristic length of the rocket, μ_{d} is the dynamic viscosity of the fluid and u is the flow velocity. This means that at greater flight speeds, the skin-friction drag experienced by a rocket becomes relatively less significant compared to the pressure-induced drag, which is the reason why extremely high speed flows can often be accurately approximated as inviscid. However, it should be noted that according to the *OpenRocket* software, skin-friction drag is a major component of the total drag experienced by a rocket for all examined freestream Mach numbers studied in this investigation.

Furthermore, the Mach number is a dimensionless quantity representing the ratio of the flow velocity past a boundary to the local speed of sound (Çengel and Cimbala, pp. 310). It is defined as

$$M = \frac{u}{c}, \tag{2}$$

where M is the Mach number, u is the flow velocity and c is the local speed of sound. For a rocket traveling at different freestream Mach numbers (denoted by M_∞ in Figure 1), the flow characteristics around the rocket can vary substantially and thus, also the magnitude of the aerodynamic forces that the rocket is subjected to. The freestream Mach number serves as an important indicator of the onset of significant changes in flow behavior. Likewise, the compressibility effects of air and the accuracy of the calorically perfect gas approximation are strongly dependent on the Mach number (Benson). In this investigation, the focus was on a rocket that travels at a freestream Mach number of 3 and below, which implies that the rocket attains subsonic, transonic and supersonic speeds. The flow behavior around a rocket traveling at each of these speeds relative to the local speed of sound is summarized in Figure 1, which is based on the flow field characterization provided in Anderson (pp. 6-7).

Subsonic Flow

Freestream:
$M_\infty < 0.8$

Locally:
$M < 1$

Transonic Flow (Low Transonic)

Freestream:
$0.8 < M_\infty < 1.0$

Locally:
$M < 1$

Normal Shock Wave

$M > 1$

Transonic Flow (High Transonic)

Freestream:
$1.0 < M_\infty < 1.2$

Locally:
$M > 1$

$M < 1$

Bow Shock

Expansion Fan

Supersonic Flow

Freestream:
$M_\infty > 1.2$

Locally:
$M > 1$

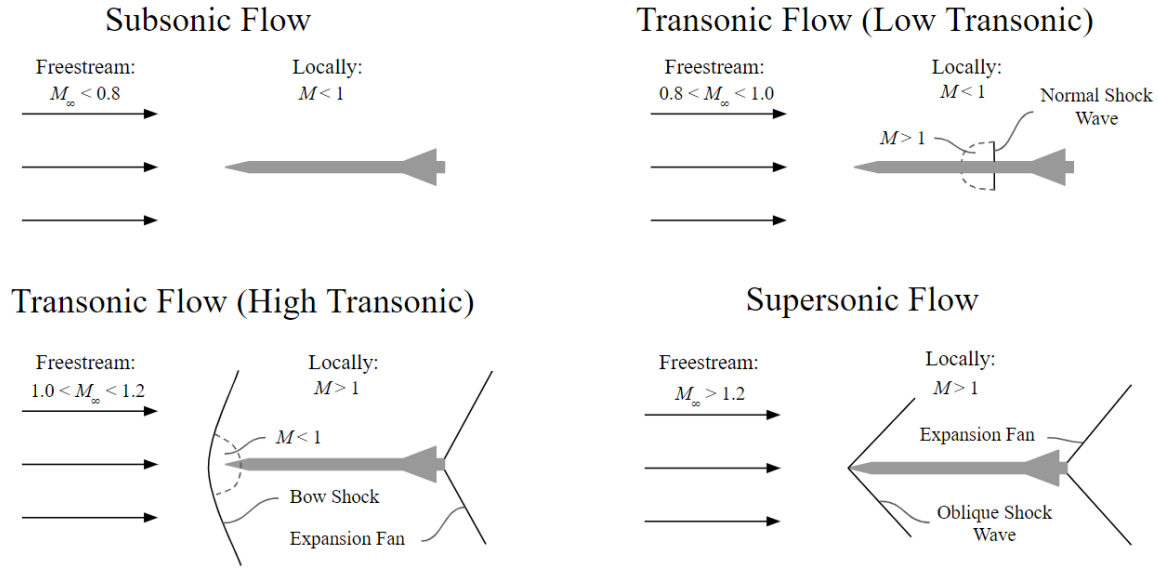Expansion Fan

Oblique Shock Wave

Figure 1: Flow behaviour around a rocket at different freestream Mach numbers, adapted from Anderson (pp. 6).

As seen in Figure 1, various aerodynamic phenomena, such as the formation of shock waves and expansion fans, depend on the rocket's freestream Mach number. As such phenomena contribute significantly to the drag experienced by a rocket, it is meaningful to classify the flow behavior based on the Mach number.

In subsonic flow, defined as $M < 1$ at every point in the flow field, the flow velocity is always below the speed of sound. As a consequence, disturbances in the flow can propagate both in the upstream and downstream direction. Also, it should be noted that $M_\infty < 1$ does not imply a perfectly subsonic flow field, since local flow velocities can surpass the freestream value and potentially become supersonic. Therefore, subsonic speeds are often approximated as $M_\infty < 0.8$ for rockets. Furthermore, it should be noted that for $M_\infty < 0.3$, the flow can often accurately be approximated as incompressible. However, for $M_\infty > 0.3$, air often experiences significant local changes in fluid density and compressibility effects are important to model, as explained in Çengel and Cimbala (pp. 11).

In transonic flow, which is characterized by having regions of both subsonic and supersonic flow, the flow behavior around the rocket changes markedly compared to perfectly subsonic flow. In particular, for transonic flows where $M_\infty < 1$, flows around the rocket can locally become supersonic, leading to normal or lambda shock waves forming at certain locations in the fluid, as shown in Figure 1. On the other hand, for transonic flows where $M_\infty > 1$, a localized region of subsonic flow is formed at the leading edge of the rocket, creating a bow shock. Additionally, the accompanying expansion of air at the trailing edge of the rocket causes expansion fans to appear. For a rocket, transonic speeds are often approximated as $0.8 < M_\infty < 1.2$, although strictly speaking this depends on the precise rocket geometry in question.

In supersonic flow, that is defined as $M > 1$ throughout the entire flow field, the flow velocity is always above the speed of sound. Hence, disturbances in supersonic flow can only propagate in the downstream direction. Likewise, supersonic flow is characterized by discontinuities in the flow field as a direct consequence of disturbances only being able to propagate downstream. Specifically, for a rocket traveling at supersonic speeds, oblique shock waves will appear at the leading edge of the rocket, whereas expansion fans will appear at the trailing edge. Supersonic speeds are often approximated as $M_\infty > 1.2$, although it depends on which freestream Mach number the bow shock reattaches with the rocket geometry to form an oblique shock wave. However, it should be noted that due to the no-slip condition for viscous fluids, the entire flow field around a rocket cannot technically be fully supersonic.

2.2   Rocket Aerodynamics

For rocket aerodynamics, arguably the most important force to examine is the drag force. As this is the main focus of this investigation, the precise definition of the drag force is provided in this section. The magnitude of the drag force is defined as

$$F_{\mathrm{D}} = \frac{1}{2} C_{\mathrm{D}} A \rho u^2, \tag{3}$$

where F_{D} is the drag force, C_{D} is the drag coefficient, A is a reference area, ρ is the fluid density and u is the speed of the object relative to the surrounding fluid (Çengel and Cimbala, pp. 309). This force is defined as parallel to the flow direction of the incoming fluid, in the reference frame of the object. For a rocket whose angular velocity is zero and whose symmetry axis is parallel to the velocity vector of the incoming fluid, which corresponds to an angle-of-attack of zero, this is the only aerodynamic force acting on a rocket. Otherwise, there will also be a lift force acting on the rocket, which is defined as perpendicular to the flow direction of the incoming fluid (Çengel and Cimbala, pp. 607). This is illustratively shown in Figure 2, where α is the angle-of-attack, F_{D} is the drag force and F_{L} is the lift force.
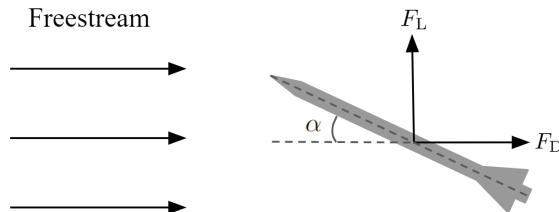

Figure 2: Aerodynamic forces acting on a rocket, adapted from Anderson (pp. 2).

3 Problem Setup

The aerodynamic drag experienced by the *Mjöllnir* rocket at different altitudes and freestream Mach numbers was examined in this investigation using CFD. This was done in order to evaluate the accuracy of the aerodynamic model employed in *OpenRocket*. This section briefly outlines how the problem was set up in *Ansys Fluent*, which is a CFD program, and *OpenRocket*, which is a rocket simulation program.

3.1 CFD Problem Setup

To solve the problem in *Ansys Fluent*, the rocket and the surrounding fluid were modeled in a virtual windtunnel environment. Specifically, the windtunnel was chosen to have a cylindrical geometry with a mass flux inlet and a pressure outlet. These boundary conditions were chosen according to the *Ansys Fluent* conventions for compressible flow (*Ansys Fluent User's Guide*, pp. 1725), that are applicable in this case due to the speeds that the rocket can travel. Also, the dimensions of the virtual windtunnel and the mesh were selected to make the computed results largely independent of these dimensions. The problem setup for the CFD simulations is illustrated in Figure 3.
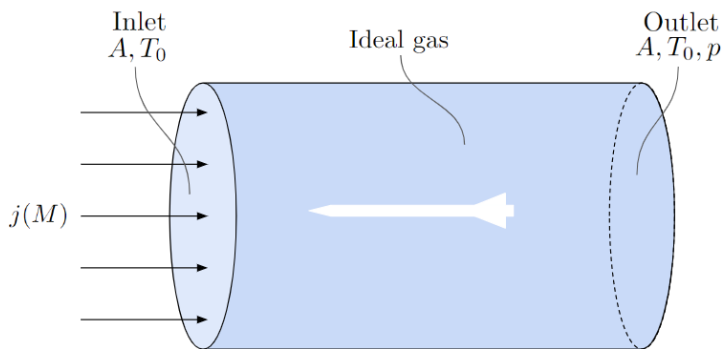
Figure 3: Problem setup for the CFD simulations.

3.2 OpenRocket Problem Setup

To solve the problem in *OpenRocket*, the rocket geometry was defined in the program and a component analysis was conducted. These were all the steps necessary to extract the rocket's drag coefficients in *OpenRocket*. Hence, no separate section was required in this report to explain the procedure. A more in-depth explanation for how the drag coefficients are calculated is provided in Niskanen (pp. 14-52). The problem setup in *OpenRocket* is demonstrated in Figure 4.
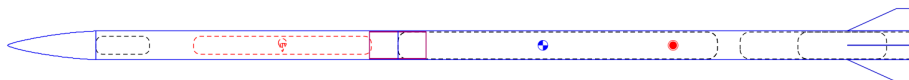
Figure 4: Problem setup for the *OpenRocket* component analysis.

4 CFD Methodology

CFD is a branch of fluid mechanics that deals with quantitatively solving fluid flow and heat transfer phenomena. It is based on the fundamental equations governing fluid flow and heat transfer, such as the Navier-Stokes equations and the equation of state.

The steps for solving a problem using CFD include:

- Preprocessing.

    - Defining and Simplifying Problem Geometry.
    - Creating Mesh.
    - Applying Material Models.
    - Assigning Boundary Conditions.

- Simulation.

    - Applying Numerical Scheme.
    - Iterative Solution Process.
    - Convergence Conditions.

- Postprocessing.

    - Verifying Convergence.
    - Verifying Physical Accuracy with Contour Plots.
    - Verifying Numerical Accuracy with Sensitivity Analyses.

4.1 Governing Equations

According to the *Ansys Fluent Theory Guide* (pp. 2-4, 16-17 & 42), the governing equations for fluid flow are derived from the Lagrangian form of the conservation of mass, energy and linear momentum for a material volume. In particular, the conservation equations are derived from an arbitrary material volume, as illustratively shown in Figure 5. In Figure 5, $\mathbf{f}$ is an intensive property, $\mathbf{v}$ is the velocity vector of the material volume, $\mathbf{F_s}$ is the net surface force acting on the material volume, $\mathbf{F_b}$ is the net volume force acting on the material volume, $\dot{Q}$ is the net heat transfer to the material volume and $\dot{W}$ is the net work done by the material volume on its surroundings.
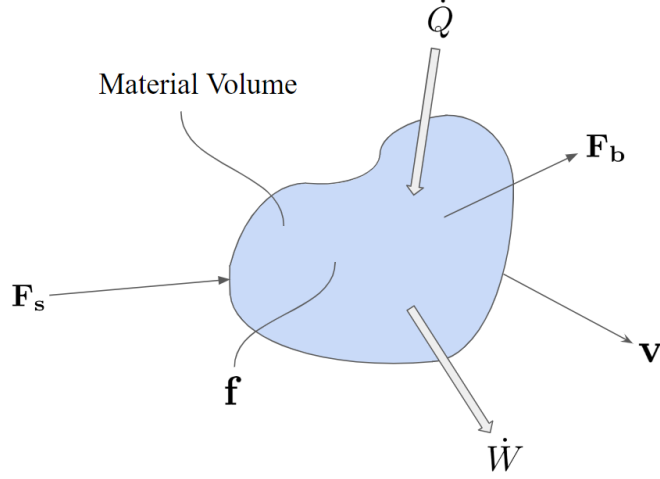
Figure 5: Arbitrary material volume.

Firstly, per definition of a material volume, there can be no mass transfer between the material volume and its surroundings. Thus, it always holds that

$$\frac{\mathrm{d}m}{\mathrm{d}t} = 0 \tag{4}$$

for a material volume, where m is the mass inside the material volume. Secondly, according to the first law of thermodynamics,

$$\frac{\mathrm{d}E}{\mathrm{d}t} = \dot{Q} - \dot{W}, \tag{5}$$

where E is the total energy inside the material volume and the remaining quantities were previously defined. Lastly, Newton's second law of motion is defined as

$$\frac{\mathrm{d}\mathbf{H}}{\mathrm{d}t} = \mathbf{F_s} + \mathbf{F_b}, \tag{6}$$

where $\mathbf{H}$ is the linear momentum of the material volume and the other variables were previously explained. To thereafter convert Equations (4), (5) and (6) to a form that is applicable for stationary control volumes such as mesh elements, Reynolds Transport Theorem is used. Reynolds Transport Theorem gives the relation between a material volume and an arbitrary control volume and can be used to convert differential equations from Lagrangian form to Eulerian form. It can be written as

$$\frac{\mathrm{d}}{\mathrm{d}t} \iiint_V \mathbf{f}\, \mathrm{d}V = \iiint_V \frac{\partial \mathbf{f}}{\partial t}\, \mathrm{d}V + \oiint_S \mathbf{f}(\mathbf{v} \cdot \hat{\mathbf{n}})\, \mathrm{d}S, \tag{7}$$

where V is the control volume, S is the surface of the control volume, $\hat{\mathbf{n}}$ is a normal vector pointing out of the control volume surface and the other variables have been defined previously. Equations (4), (5), (6) and (7) combined make up the Navier-Stokes equations that govern fluid flow and heat transfer phenomena in *Ansys Fluent*. However, turbulent flows can often not be solved directly using

the Navier-Stokes equations, since solving such problems is prohibitively computationally intensive due to the complex mixing phenomena involved in turbulent flows. Therefore, a Reynolds-Averaged Navier-Stokes (RANS) turbulence model was used in this investigation to be able to solve the CFD problem with the computational resources available. More specifically, the k-ω SST turbulence model was employed, because research by López et al. (pp. 340) suggests that it is the most appropriate RANS model for rocket aerodynamics and the *Ansys Fluent User's Guide* (pp. 2012) also recommends this particular model for aerodynamic flows.

In *Ansys Fluent*, the Navier-Stokes equations are solved using a finite volume method (*Ansys Fluent Theory Guide*, pp. 42-43). This method involves dividing the fluid domain into discrete control volumes (defined by the mesh), integrating the Navier-Stokes equations for each individual control volume to obtain a set of algebraic equations and linearizing the algebraic equations to obtain a discrete linear equation system to solve. When this system is solved, the solution is updated and the process is iteratively repeated until the solution has converged. In this investigation, the total drag force on the rocket could be calculated by summing together each individual contribution from the mesh elements adjacent to the rocket body.

4.2   Material Properties

Two regions were assumed to have distinct material properties in this investigation, namely, the solid region comprising the rocket geometry and the fluid region comprising the surrounding air. As such, the material properties of these two regions were modeled distinctly in *Ansys Fluent*.

Firstly, the rocket geometry was assumed to behave as a rigid body, meaning that aeroelastic effects were neglected. This was done to simplify the overall aerodynamic analysis. It should be noted that the *Mjöllnir* rocket has been dimensioned to prevent it from experiencing any significant deformations during flight, which is why this assumption is mostly accurate. Likewise, it was assumed that the rocket geometry can be approximated as a perfectly thermally insulated body. This was done to reduce the complexity of the problem and make it simpler to run the CFD simulations. The rocket geometry was modeled as a dead zone in *Ansys Fluent*, which implies that the geometry acts as a thermally insulated static wall.

Secondly, the air was modeled as a calorically perfect gas in this investigation, where the gas was assumed to be both compressible and viscous. Note that for a calorically perfect gas, the ideal gas law always holds. The heat capacity ratio is always constant for such idealized gases and the speed of sound can, according to Çengel and Cimbala (pp. 663), be expressed as

$$c = \sqrt{\gamma R^* T}, \tag{8}$$

where T is the local temperature and the other parameters are explained in Table 16 of Appendix B. The air was assumed to behave as a calorically perfect gas, since real gases subject to subsonic or supersonic flow are accurately modeled as such (Benson). Compressibility was assumed because rockets traveling at $M_\infty > 0.3$ tend to cause significant local density variations in the surrounding air, as explained in Çengel and Cimbala (pp. 11). Moreover, the air was assumed to be viscous, because according to the *OpenRocket* results, friction drag accounts for a significant component of the total drag experienced by the *Mjöllnir* rocket at all freestream Mach numbers examined in this

investigation. Thus, the air was assumed to adhere to Sutherland's law, which implies that the local viscosity of the air is given by

$$\mu = \frac{T_0 + C}{T + C} \left(\frac{T}{T_0} \right)^{3/2} \mu_0,$$

(9)

where μ is the viscosity, μ_0 is a reference viscosity, T_0 is a reference temperature and C is the Sutherland constant (*Ansys Fluent User's Guide*, pp. 1600). Specifically, the preset values for Sutherland's law in *Ansys Fluent* were used. Otherwise, the gas parameters were set to standard sea-level conditions, as specified in Table 16 of Appendix B, or calculated using the International Standard Atmosphere (ISA) model for the troposphere (also specified in Appendix B) using ISO 2533:1975 (pp. 1-5).

4.3 Geometry and Mesh Preparations

The rocket geometry that was examined in this investigation was the *Mjöllnir* rocket built by *ÆSIR*, illustratively shown in Figure 6. However, since the stated aim of this investigation was to evaluate the accuracy of the *OpenRocket* model, certain simplifications of the true rocket geometry were made to imitate the simplified rocket geometry implemented in *OpenRocket*. Furthermore, such simplifications help enhance the numerical stability of the simulation and reduce the overall required cell count of the mesh. Therefore, the *Mjöllnir* geometry was simplified by removing the pitot tube at the front, slightly rounding the nose cone at the tip, not accounting for the slight diameter variations along the rocket, removing the rocket's fins, strongly simplifying the rocket engine nozzle geometry and assuming a perfectly axisymmetric body. As a consequence, since both the rocket geometry and the fluid flow in the problem were assumed to be axisymmetric, the problem itself could be solved in two dimensional space, rendering a full three dimensional analysis unnecessary.

Figure 6: Full *Mjöllnir* rocket geometry.

Additionally, to generate a mesh of sufficient quality for use in the CFD simulations, both the global and local mesh properties were carefully chosen. Likewise, the quality of the generated mesh was evaluated both through inspection and checking its quality statistics. This was done to determine whether the mesh would likely produce accurate results if used in the CFD simulation, especially since testing this through trial and error was quite computationally intensive.

In this investigation, an unstructured mesh was used to model the fluid domain instead of a structured mesh. This was done to be able to accurately capture the relatively complex geometry at the trailing edge of the rocket, as well as avoid creating cells with high aspect ratios when transitioning between regions of different cell sizes. Furthermore, a quadrilateral-dominant mesh was chosen because the net flow direction in the problem is perfectly aligned with the rocket symmetry axis. This implies that a quadrilateral-dominant mesh captures the flow behavior more accurately than a triangular mesh. Moreover, inflation layers were added to properly account for the rocket's boundary layer without generating excessively many cells adjacent to the rocket wall. Inflation layers can often have cells with relatively high aspect ratios, meaning that fewer cells need to be used, without necessarily destabilizing the CFD simulation or giving rise to unphysical solutions. This can be attributed to the tangential velocity component of the flow close to a no-slip wall being relatively small and the normal velocity component being insignificant. However, to find a balance between excessively high aspect ratios and a too great cell count, the dimensionless first cell height parameter was chosen as $30 < y^+ < 300$ for all freestream Mach numbers examined in this investigation. This specific range of y^+ values was chosen, because the k-ω SST turbulence model is compatible with using data from the log-law zone of the boundary layer when a wall-function is employed. Likewise, in *Ansys Fluent*, the implementation of the k-ω SST model is largely y^+ insensitive, since it uses a combination of wall functions (*Ansys Fluent User's Guide*, pp. 2018). Additionally, the *Ansys Fluent User's Guide* (pp. 2018) places greater importance on using at least ten inflation layers within the boundary layer and having the total inflation layer thickness exceed the boundary layer thickness, rather than strictly achieving a specific y^+ value. Therefore, thirty inflation layers were added to the mesh with a growth rate of 1.2 and a first cell height of $5\,\mu m$. Moreover, to ensure a smooth transition between the inflation layer and the surrounding cells, a local cell sizing of $1\,mm$ was applied to the edge of the rocket wall. However, no inflation layers were added to the wall of the rocket engine nozzle, because this investigation focused on a rocket with an inactive propulsion system. Thereby, the air is almost completely static near the wall of the nozzle and simulations showed that high aspect ratio cells in its vicinity could cause the solution to become unstable and diverge. Therefore, the inflation layers had a highly skewed geometric cell height distribution up to the point where the shear layers begin to form and were thereafter made to gradually transition to having a completely uniform cell height distribution. Specifically, the inflation layers were terminated at a perpendicular bend before the nozzle was reached, as shown in Figure 7. Note that no particular cell sizing adjustments were made for the shear layers in this investigation, which implies that this feature might not have been fully resolved in the simulations.
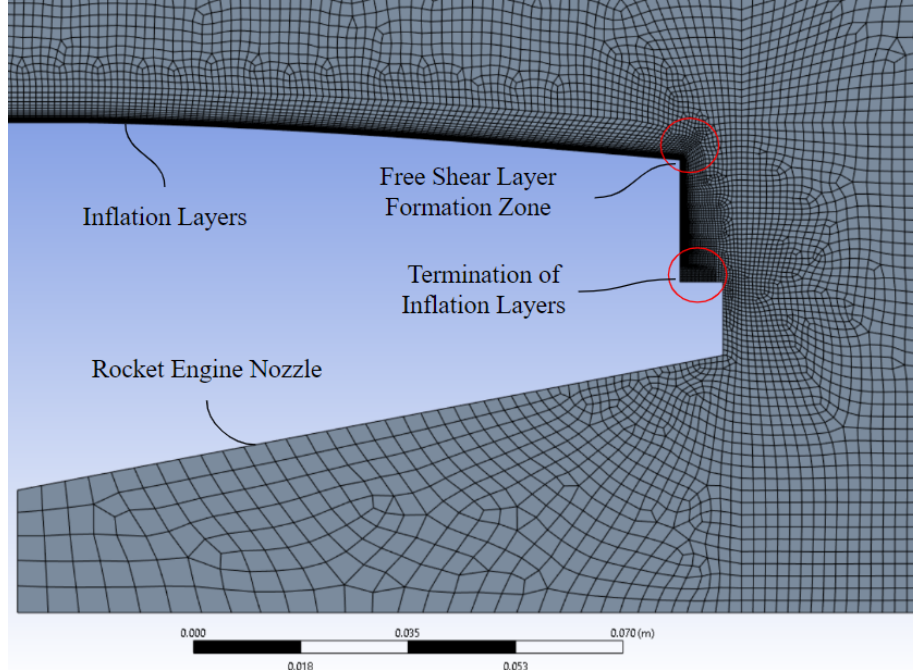
Figure 7: Mesh of inflation layers in the fluid domain.

Furthermore, to reduce the total required cell count, the fluid domain was split into distinct regions, as shown in Figure 8. This allowed for separate local cell sizes to be applied to different regions of the fluid domain and this was useful for generating a mesh with cell sizes that resolved all important local flow phenomena in each distinct region. Specifically, smaller cell sizes were required close to the rocket and larger cell sizes could be used further away from the rocket where there existed no significant gradients in the solution.
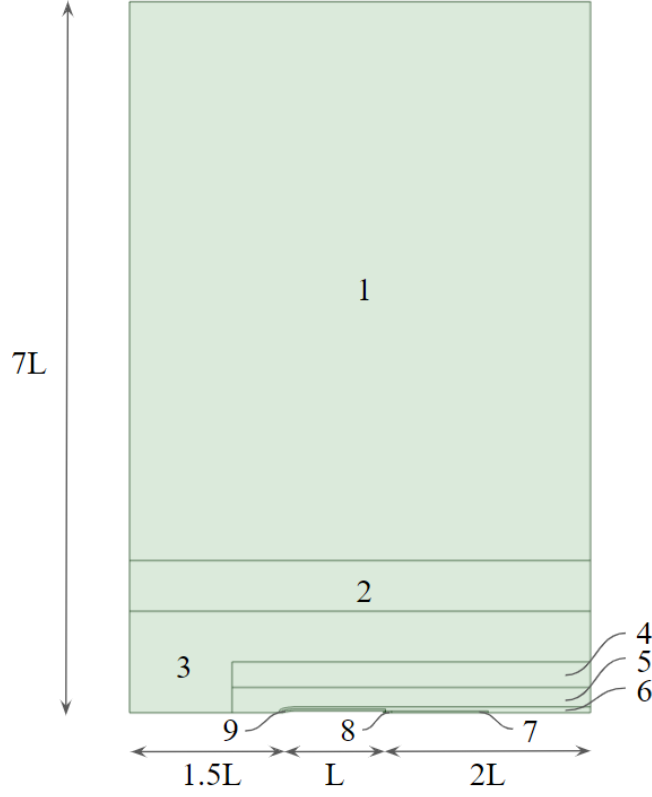
Figure 8: Fluid domain geometry.

The local sizing in each fluid region that is specified in Figure 8 is given in Table 1.

Table 1: Local size adjustments

Fluid Region	Size Adjustment	Element Size [mm]
1	Local Face Sizing	1280
2	Local Face Sizing	160
3	Local Face Sizing	40
4	Local Face Sizing	30
5	Local Face Sizing	20
6	Local Face Sizing	10
7	Local Face Sizing	6
8	Local Face Sizing	2
9	Local Edge Sizing	1

Ultimately, to capture local flow phenomena as well as possible and avoid unphysical effects in the solution, a relatively low global growth rate of 1.05 was chosen. Likewise, curvature capture was enabled globally with a minimum element size of $0.5\,\mathrm{mm}$ to properly account for the curvature

of the rocket. In fluid regions 1 and 2, the local element sizes chosen were relatively large to artificially dissipate the shock waves in these regions and prevent shock wave reflections off the virtual windtunnel's walls. The reason for this was that the computational resources required to perfectly resolve the shock waves in fluid regions relatively far away from the rocket geometry were not available. The generated mesh for the entire fluid domain is shown in Figure 9.

Figure 9: Mesh of the fluid domain.

Due to the vast differences in scale between the entire fluid domain and the rocket geometry, a close-up of the meshed fluid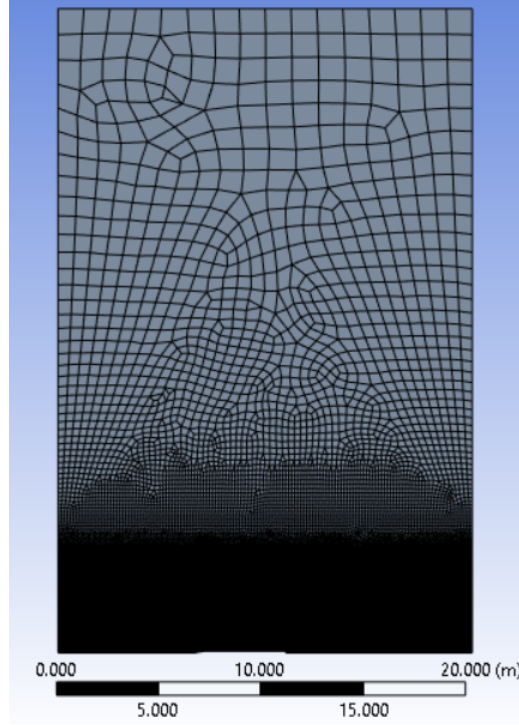 domain around the rocket geometry is also displayed, in Figure 10. The purpose of this is to visually clarify the geometric simplifications made for the *Mjöllnir* rocket geometry and the results of the local sizing adjustments mentioned in Table 1.
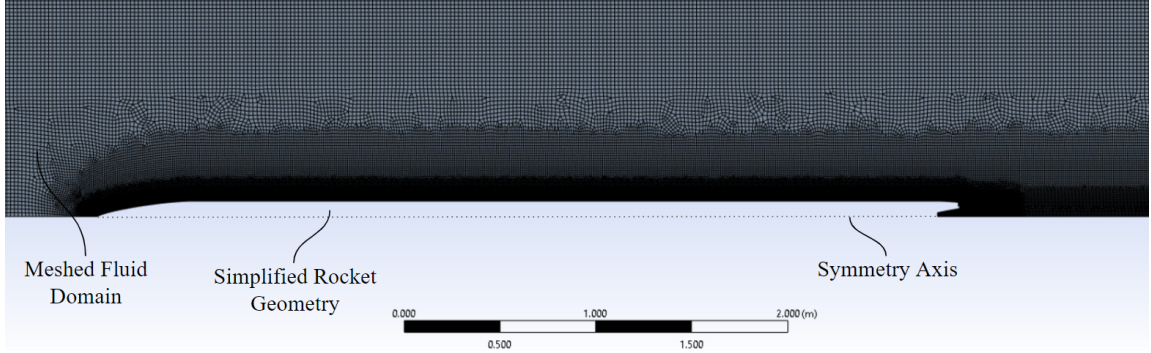
14

Figure 10: Mesh of the fluid domain close to the *Mjöllnir* rocket.

Lastly, the risk of failure for the generated mesh was examined by checking if the minimum orthogonal quality, maximum skewness and maximum aspect ratio of the mesh cells were within acceptable levels. The final mesh had a minimum orthogonal quality of 0.085, a maximum skewness of 0.86 and a maximum aspect ratio of 231, for cells adjacent to the rocket wall. According to the *Ansys Fluent User's Guide* (pp. 1115-1116), it is recommended to have a minimum orthogonal quality above 0.01, a maximum skewness below 0.95 and a maximum aspect ratio of 10 for cells inside a boundary layer. However, the generated mesh produced stable and sensible results in all simulations run. Therefore, it was concluded that the lowest quality cells did not meaningfully affect the solution's convergence or the final solution obtained.

4.4 Sensitivity Analyses

To properly dimension the fluid domain mesh for the CFD simulations, many factors had to be considered. In particular, the fluid domain dimensions, the cell sizes and mesh distribution had to be chosen appropriately to make the results largely independent of these parameters. As a direct consequence, multiple sensitivity analyses were conducted to ensure both that the results became independent of the chosen parameters and that the final mesh did not have needlessly many cells.

The height of the virtual windtunnel was dimensioned in two stages. First, the domain height was increased until unphysical shock wave reflections at the walls of the virtual windtunnel could not be observed in the solution's contour plots. Secondly, the height was further increased until the percentage change of the drag force with respect to the percentage change in the height dimension was less than 1 %, or explicitly

$$\text{Relative Change} = \frac{\frac{|F_{\text{D},i+1}-F_{\text{D},i}|}{F_{\text{D},i}}}{\frac{|D_{i+1}-D_i|}{D_i}} < 1\,\%, \tag{10}$$

where D is the relevant exterior dimension or cell count being altered, F_{D} is the drag force and i is the relevant row index in Tables 2 to 5. In particular, the fluid domain height was increased until the computed drag force was largely independent of this dimension, as shown in Table 2.

Table 2: Domain height sensitivity analysis

Dimension [mm]	Drag Force [N]	Relative Change
13500	697	5.82 %
18000	687	5.04 %
22500	694	3.57 %
31500	687	0.66 %
40500	686	-

Thereafter, the upstream and downstream dimensions of the virtual windtunnel were chosen to make the results largely independent of these exterior dimensions, as shown in Tables 3 and 4.

Table 3: Upstream length sensitivity analysis

Dimension [mm]	Drag Force [N]	Relative Change
4500	682	2.18 %
6750	687	0.58 %
9000	686	-

Table 4: Downstream length sensitivity analysis

Dimension [mm]	Drag Force [N]	Relative Change
9000	688	0.44 %
13500	687	-

Lastly, the cell sizes were adjusted by roughly doubling the amount of cells each iteration, which corresponds to changing each local size adjustment, as specified in Table 1, by a factor of $\frac{1}{\sqrt{2}}$. Thus, a final cell count of 315444 was obtained, as shown in Table 5.

Table 5: Cell size sensitivity analysis

Cell Count	Drag Force [N]	Relative Change
190719	687	1.01 %
315444	690	0.98 %
568921	687	-

Hence, the final dimensions for the fluid domain were a domain height of 31500 mm, an upstream dimension of 6750 mm and a downstream dimension of 9000 mm, as shown in Figure 8, where $L = 4500$ mm. Likewise, important local size adjustments are shown in Table 1.

4.5   Boundary Conditions

To obtain robust and stable numerical results, the inlet and outlet boundary conditions were set according to the recommendations in the *Ansys Fluent User's Guide* (pp. 1725). Specifically, as real gases are compressible for most inlet Mach numbers examined in this investigation, a mass flux inlet and pressure outlet was used. To properly set the inlet boundary condition, the mass flux was calculated according to Equation (11), where

$$j = \frac{\dot{m}}{A} = \rho\sqrt{\gamma R^* T} \cdot M. \tag{11}$$

In Equation (11), j denotes the mass flux, $\dot{m}$ is the mass flow rate, A is the inlet area and the other quantities are described in Table 16 of Appendix B and Equation (2). In deriving this equation, it was assumed that the air at the inlet has a constant density. It was also assumed that the air behaves as a calorically perfect gas, which implies that the speed of sound is given by Equation (8). For the outlet boundary condition, the pressure was set to standard atmospheric pressure, that is specified in Table 16 of Appendix B, or calculated using the ISA model of the atmosphere (also detailed in Appendix B). Due to the fact that *Ansys Fluent* also requires information about the total temperature in the inlet and outlet boundaries, this quantity was calculated for each inlet Mach number (Çengel and Cimbala, pp. 668) using Equation (12), where

$$T_0 = \left(1 + \frac{\gamma - 1}{2}M^2\right) T. \tag{12}$$

In Equation (12), T_0 denotes the total temperature, T is the ambient air temperature and the other quantities are detailed in Table 16 of Appendix B and Equation (2). It should be noted that this equation is only valid for a calorically perfect gas, which was assumed to be an accurate approximation for the Mach regimes examined in this investigation. Additionally, it was required to specify the turbulence intensity and turbulent viscosity ratio at the inlet and outlet. As a consequence of there not existing any exact guidelines for how to specify these parameters for a rocket traveling at different altitudes, the turbulence at the boundaries was always assumed to be low. Note that, in general, the freestream boundaries of external flows have low turbulence and therefore, the turbulent viscosity ratio was set to 5, which is a common value for said boundary conditions, according to the *Ansys Fluent User's Guide* (pp. 1362-1363). Likewise, the turbulence intensity was chosen as 1 %, that is generally considered characteristic for "low" turbulence (*Ansys Fluent User's Guide*, pp. 1361). Through experiment, it was found that drastically changing the turbulence at the boundaries did not affect the results by more than 0.2 % at a freestream Mach number of 1.0.

The interface between the rocket geometry and the surrounding fluid was set to a no-slip wall boundary condition, whereas the wall of the virtual windtunnel was set to a symmetry boundary condition. A symmetry boundary condition was chosen instead of free-slip wall, because these two boundary conditions are roughly equivalent in *Ansys Fluent*. Likewise, simulations showed that a free-slip wall boundary condition implied a risk of getting unphysical turbulent kinetic energy production at this surface due to poor boundary layer resolution. However, a proper boundary layer resolution is not required at this surface, since it is in reality not a physical wall, but rather a finite approximation for air that is sufficiently far away from the rocket not to be disturbed by its bypassing. Lastly, the symmetry axis of the rocket was set to an axis boundary condition, because both the flow and the simplified rocket geometry in this investigation were axisymmetric.

4.6 Numerical Considerations and Solver Setup

To solve the CFD problem in *Ansys Fluent*, an axisymmetric, steady-state, density-based solver was used. Specifically, a density-based solver was used because compressibility effects are significant for most freestream Mach numbers examined in this investigation. Furthermore, a steady-state solver was used because it is faster to run than a transient solver and transient effects do not strongly affect the final solution. This was verified by running a few transient simulations with the exact same setup as the steady-state simulations. The results differed by less than 4 %, although the simulation time was significantly longer for the transient solver and therefore, it was decided to be more prudent to use the steady-state solver.

Additionally, to avoid the possibility of having the simulations diverge due to overly large Courant-Friedrichs-Lewy (*CFL*) number, the Roe-FDS implicit solver was used. Specifically, the *CFL* number is a necessary condition for convergence in numerical simulations that involve solving partial differential equations with an explicit numerical scheme. However, the *CFL* number is also an important parameter for CFD simulations solved using an implicit numerical scheme, since it determines the required simulation time, accuracy and stability of the results. It is defined as

$$CFL = \Delta t \left(\sum_{i=1}^{n} \frac{u_i}{\Delta x_i} \right) \leq CFL_{\max}, \tag{13}$$

where Δt is the time step, u_i is the magnitude of the velocity in the i direction of the coordinate system, Δx_i is the length interval in the i direction of the coordinate system and $CFL_{\max}$ is the maximum possible *CFL* number before the solution diverges (Courant et al., pp. 215-234). As most of the simulated scenarios in this investigation involved high Mach number compressible flows, the convergence of the solution could be quite sensitive to the *CFL* number, especially in the first hundreds of iterations before the flow field had begun to stabilize. Therefore, FMG initialization was enabled to improve the initial "guess" of the flow field and solution steering was enabled to dynamically adjust the *CFL* number based on the solution's level of convergence and whether the flow field was chiefly subsonic, transonic or supersonic. Furthermore, to aid the convergence of the solution, the temperature limit for all cells in the mesh was set to a maximum of 200 K above the stagnation temperature which was calculated using Equation (12). Simulations showed that the final converged solutions were not affected by this limit, but it helped the solutions converge faster.

Lastly, for the spatial discretization scheme, the turbulent kinetic energy and specific dissipation rate were set to second order upwind, whereas the flow was set to first order upwind. The reason for setting the flow to first order upwind was that the second order upwind scheme produced unphysical fluctuations of various quantities at certain locations in the flow field. However, to ensure that this simplification did not adversely affect the solution, a simulation with a second order upwind flow scheme and a transient solver was run. This was because it was assumed that these fluctuations were the result of averaged transient effects being "smeared out" in the steady-state solution. In the transient simulation, the fluctuations had almost completely disappeared and the contour plots were vastly more similar to the contour plots of the steady-state first order upwind flow scheme than the second order one. The same held true for the computed drag force in the simulation, which implies that the first order scheme likely provided a better approximation of the true solution. This is likely a consequence of the flow field in the problem being largely aligned with the generated quadrilateral mesh grid, for which first order schemes are well suited for (*Ansys Fluent User's Guide*, pp. 3510).

5 Results

The results of the CFD simulations in *Ansys Fluent* and the drag coefficients extracted from *Open-Rocket* are summarized in this section.

5.1 Verifying Physical Accuracy with Contour Plots

To verify that the results correspond with theory and that the solver setup in *Ansys Fluent* was correct, the contour plots of the *Mjöllnir* rocket were examined for each characteristic flow regime mentioned in Figure 1. To make the observed flow behavior clearer, the lower boundaries of the plotted Mach numbers were adjusted in the contour plots. Thereby, the lower boundaries also encompass all values below the stated Mach number in Figures 11, 12, 13 and 14. For all the aforementioned Figures, the wake region can clearly be seen at the trailing edge of the rocket and the boundary layer may be observed at close inspection by the rocket wall. However, the boundary layer is admittedly clearest in Figures 12 and 13, due to the relatively narrower range of Mach numbers plotted.

Specifically, Figure 11 shows the flow field around the *Mjöllnir* rocket when it travels at a freestream Mach number of 0.4. For rockets traveling at subsonic speeds, it is true that $M < 1$ at every point in the flow field and thus, the flow velocity is always below the speed of sound. This flow characteristic can also be observed in Figure 11 by examining the Mach number scale.

Figure 11: Contour plot of *Mjöllnir* traveling at a freestream Mach number of 0.4.

Figure 12 shows the flow field around the *Mjöllnir* rocket when it travels at a freestream Mach number of 0.9. As seen in the Figure, the Mach number is $M < 1$ everywhere, except in a small region close to the leading edge of the rocket where $M > 1$ and a normal shock wave appears. This can be expected for transonic flows where $M_\infty < 1$ as highlighted in Figure 1.

Figure 12: Contour plot of *Mjöllnir* traveling at a freestream Mach number of 0.9.

Figure 13 shows the flow field around the *Mjöllnir* rocket when it travels at a freestream Mach number of 1.1. For transonic flows where $M_\infty > 1$, a localized region of subsonic flow is formed at the leading edge of the rocket, creating a bow shock. Likewise, the expansion of air at the trailing edge of the rocket causes expansion fans to appear, as shown in Figure 1. Both of these phenomena are clearly observed in Figure 13, suggesting that the problem setup is accurate, since the converged solution agrees well with theory.
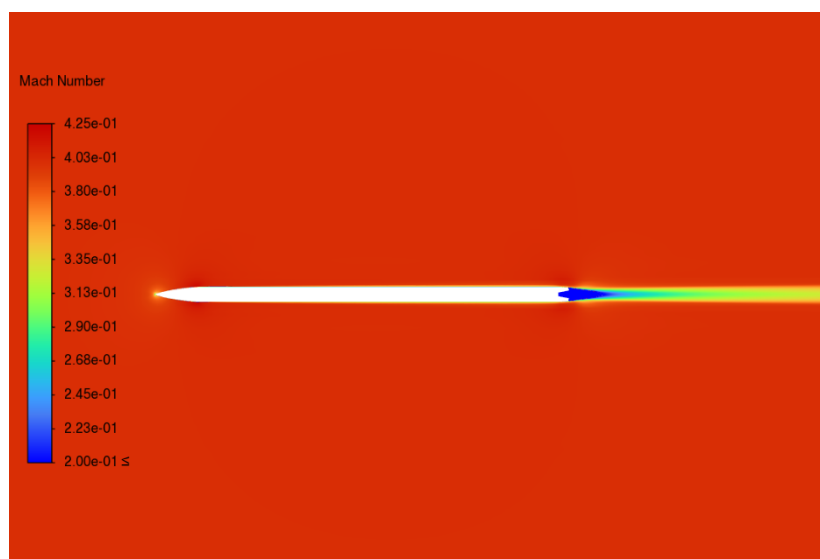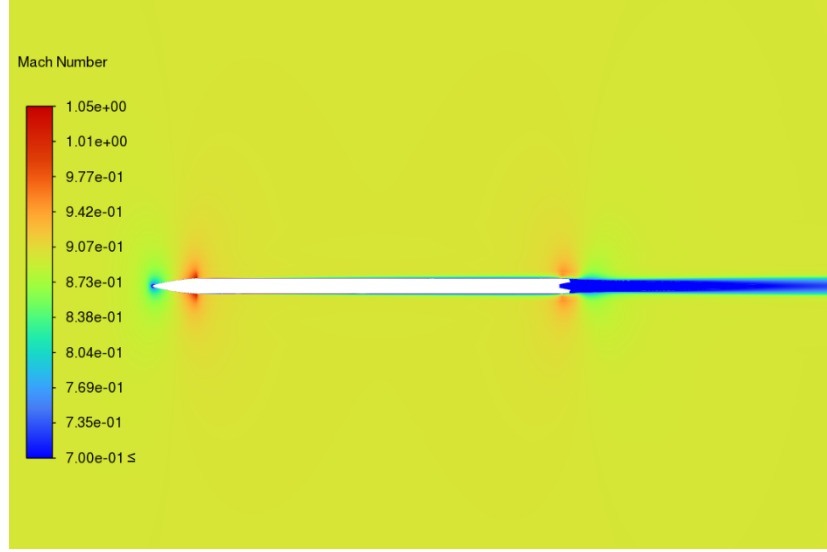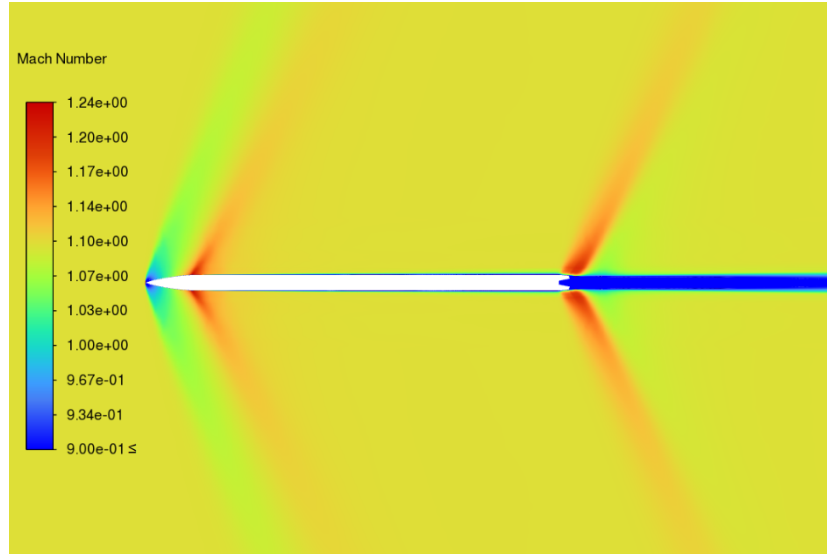

Figure 13: Contour plot of *Mjöllnir* traveling at a freestream Mach number of 1.1.

Figure 14 shows the flow field around the *Mjöllnir* rocket when it travels at a freestream Mach number of 2.0. Specifically, for a rocket traveling at supersonic speeds, oblique shock waves will appear at the leading edge of the rocket, whereas expansion fans will appear at the trailing edge. This can evidently be seen Figure 14.
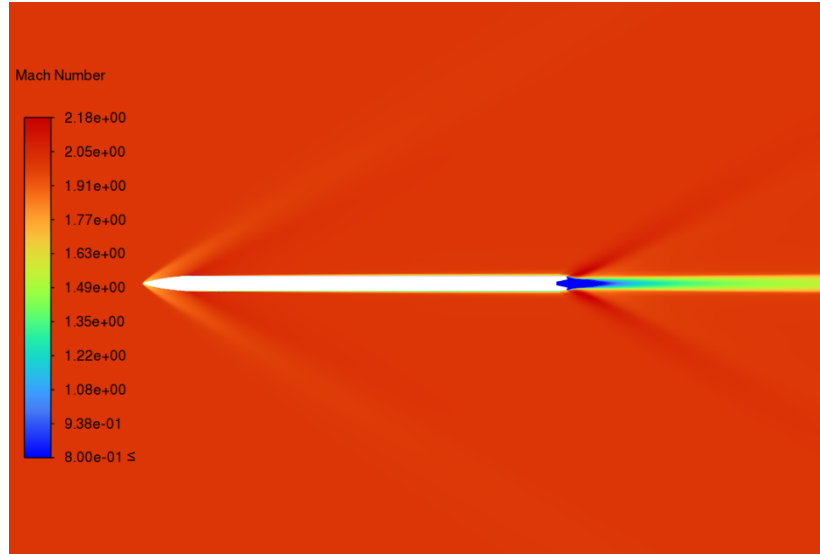

Figure 14: Contour plot of *Mjöllnir* traveling at a freestream Mach number of 2.0.

By comparing Figures 11, 12, 13 and 14 to Figure 1, it is clear that all aerodynamic phenomena expected from theory are observed in the contour plots extracted from the simulations. This strongly indicates that the results are physically accurate and that the problem was properly set up.

5.2 Verifying Numerical Accuracy with Convergence

To verify that the final solution was numerically accurate and had fully converged for each of the simulations, both the drag force plot and the residuals plot were qualitatively examined. Likewise, a simulation stopping condition was activated if all studied residuals fell below $1 \cdot 10^{-10}$ of their normalized initial values. Often, the residuals did fall below this value and therefore the solution could be considered essentially exact. However, for the least converged simulation, the greatest residual was the y-velocity where the value continuously oscillated, although the mean value stopped changing and it had a peak value of $4 \cdot 10^{-4}$, as shown in Figure 15. Note that as a rule of thumb, a maximum residual of $1 \cdot 10^{-3}$ is often considered to be a converged solution in *Ansys Fluent*. However, it is often more relevant to examine that the quantity of interest, in this case the drag force, does not change for each successive iteration. Therefore, it was ultimately the plot of the computed drag force that was mainly used to verify convergence. Again, this value was often exact to at least four decimal places, where the drag was given in Newtons. However, for the least converged simulations, this value oscillated by ± 0.001 N. Therefore, in these situations, the drag force was calculated as a mean value of the last 50 iterations and rounded to three decimal places. Overall, this implies that the random error in this investigation was exceptionally low.
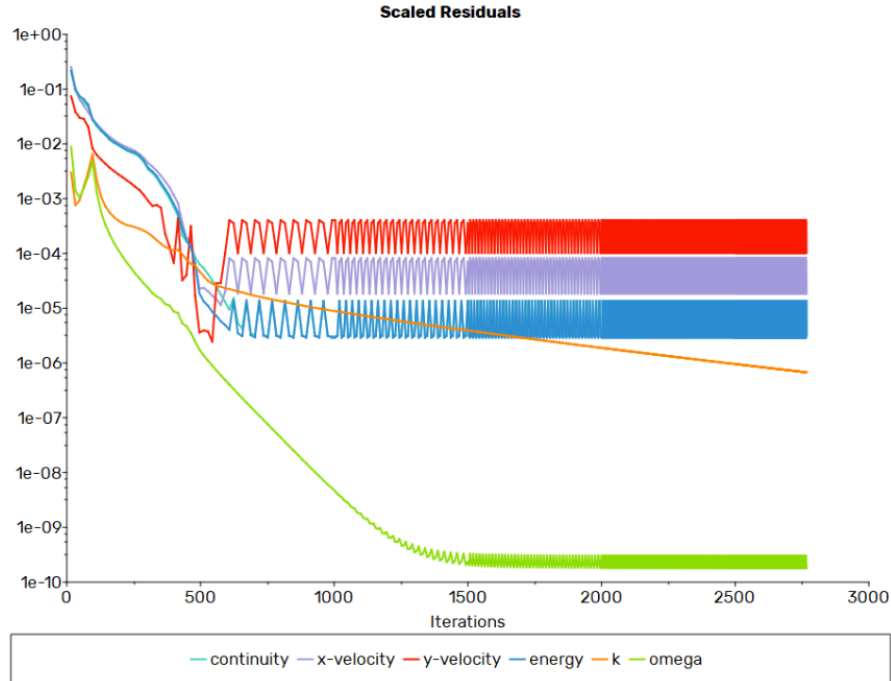

Figure 15: Residuals plot of the least converged simulation.

5.3 Comparison of Results

The drag coefficients calculated by the *OpenRocket* software for the *Mjöllnir* rocket geometry are given in Table 8 of Appendix A. Likewise, using *Ansys Fluent*, the drag coefficients were obtained by taking the computed drag forces at each respective altitude in Tables 9, 10, 11, 12 and 13 of Appendix A, combined with the atmospheric model in Appendix B. Specifically, this data was inset into Equation (3), where the reference area was provided in *OpenRocket* as $0.0201\,\mathrm{m}^2$, to calculate the *Ansys Fluent* drag coefficients for the *Mjöllnir* rocket. Figure 16 presents a direct comparison of the plotted *OpenRocket* and *Ansys Fluent* drag coefficients for the *Mjöllnir* rocket as a function of the freestream Mach number.
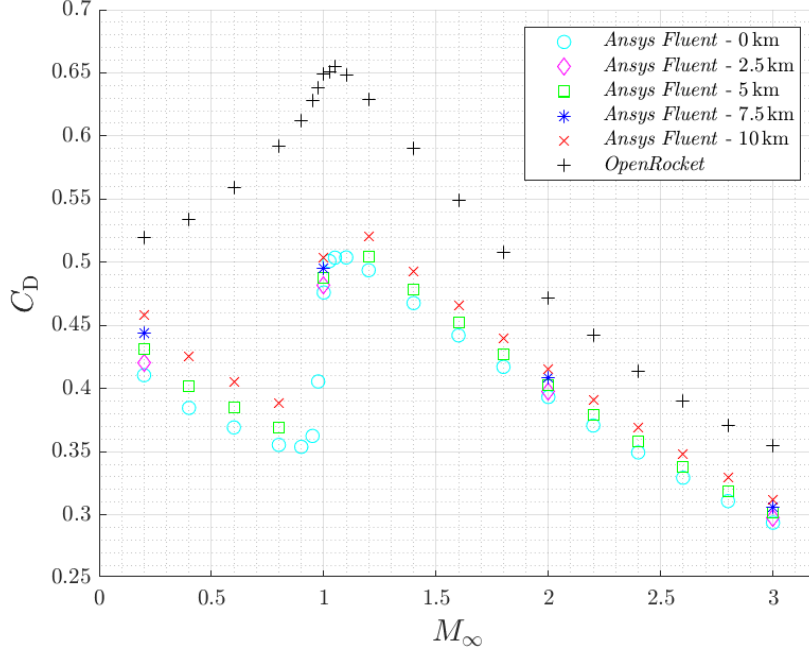
Figure 16: Plot of drag coefficients as a function of the freestream Mach number.

As shown in Figure 16, *OpenRocket* consistently overpredicts the drag force experienced by the *Mjöllnir* rocket by $12\,\%$ to $73\,\%$ for all examined freestream Mach numbers and altitudes. Likewise, there seems to be a clear systematic error when *OpenRocket* calculates the drag coefficient in the $0.2 \leq M_\infty \leq 0.8$ range, since it predicts that the drag coefficient monotonically increases in this range, whereas the CFD simulations suggest a monotonic decrease. However, *OpenRocket* seems to provide relatively more accurate predictions for the drag coefficients in the supersonic range compared to its subsonic and transonic ranges, even though its drag coefficients are always overestimates. Note that both the drag coefficient of the V-2 rocket (Mian et al., pp. 142) and the Saturn V rocket (Sagliano, pp. 3) vary with the freestream Mach number similarly to the CFD-computed drag coefficients of the *Mjöllnir* rocket. Furthermore, *OpenRocket* relies on semi-empirical formulae that often depend on relatively unrealistic and idealized assumptions about the flow behavior around a rocket to estimate the drag coefficients. Therefore, it was judged that the *Ansys Fluent* results were more accurate than the *OpenRocket* results.

6 Empirical Drag Coefficient Model

Based on the trends observed in Figure 16 for the calculated drag coefficients in *Ansys Fluent*, it was hypothesized that the drag coefficients at different altitudes could be written as the sum of the drag coefficient at sea-level conditions (denoted $C_{\mathrm{D,\ Sea\text{-}Level}}$) and an altitude correction factor (denoted ΔC_{D}).

$$C_{\mathrm{D}}(h, M_\infty) = C_{\mathrm{D,\ Sea\text{-}Level}}(M_\infty) + \Delta C_{\mathrm{D}}(h, M_\infty), \tag{14}$$

where h is the altitude of the rocket above sea-level and M_∞ is the freestream Mach number. Thereafter, by taking the difference of the drag coefficients at sea-level with the drag coefficients at higher altitudes and carefully examining the data, it was hypothesized that the altitude correction factor could empirically be expressed as

$$\Delta C_{\mathrm{D}}(h, M_\infty) = h(c_1 h + c_2) M_\infty^{c_3}, \tag{15}$$

where c_1, c_2 and c_3 are empirical coefficients. By performing a nonlinear least-squares regression in *MatLab*, the function of best-fit for Equation (15) was determined explicitly. Both the data points and the function of best-fit were plotted in the same graph using *MatLab*. The graph is displayed in Figure 17.

Figure 17: Plot of the regression model for the altitude correction factor.

Specifically, the red crosses in Figure 17 represent the data points at $10\,\mathrm{km}$, the blue asterisks represent the data points at $7.5\,\mathrm{km}$, the green squares represent the data points at $5\,\mathrm{km}$ and the magenta diamonds represent data points at $2.5\,\mathrm{km}$. Likewise, the surface represents the fitted

24

function. By inspection, it appears as though the regression model marginally overpredicts the difference in the drag coefficients at $2.0 < M_\infty < 3.0$ and marginally underpredicts the difference at $0.4 < M_\infty < 1.0$. According to model statistics, the root mean square error was 0.000932 and the p-value was $1.13 \cdot 10^{-47}$. Additionally, all model coefficients were determined to be statistically significant, because the maximum coefficient p-value was determined to be $2.02 \cdot 10^{-10}$, which is significantly less than the 1% threshold used in this investigation to discard the coefficient. It should be noted that this empirical interpolation model was determined for the *Mjöllnir* rocket using the ISA model of the troposphere and should be treated only as valid for $h \leq 10\,\mathrm{km}$ and $0.2 \leq M_\infty \leq 3.0$. Exact coefficient values and statistics are given in Table 6.

Table 6: Empirical coefficient values for the altitude correction factor

Coefficient	Estimate	Units	p-value
c_1	$8.54 \cdot 10^{-5}$	km^{-2}	$2.02 \cdot 10^{-10}$
c_2	$1.96 \cdot 10^{-3}$	km^{-1}	$2.36 \cdot 10^{-22}$
c_3	-0.357	-	$8.41 \cdot 10^{-33}$

However, in reality, it is not the altitude itself that affects the drag coefficient, but rather (most likely) the Reynolds number that itself varies with altitude. Despite this, it was determined that the empirical relation as a function of the Reynolds number and freestream Mach number would be more complicated to model compared to Equation (15), since both the Reynolds number and the freestream Mach number vary with the speed of the rocket.

Thereafter, by carefully examining the data for the drag coefficients of the *Mjöllnir* rocket at sea-level conditions, it was found that the drag coefficients in the subsonic and supersonic ranges respectively could almost perfectly be fitted with quadratic equations. There did not appear to exist any simple equation to express the data in the transonic range however. Therefore, it was reasoned that a logistic growth function with a minimum value of 0 and maximum value of 1 could be used to smoothly transition from the subsonic range of drag coefficients to the supersonic range. Thus, after rearranging the aforementioned relationship, it was hypothesized that the drag coefficients at sea-level conditions could be empirically expressed as

$$C_{\mathrm{D,\ Sea\text{-}Level}}(M_\infty) = \frac{(k_1 + k_2 M_\infty + k_3 M_\infty^2) + (k_4 + k_5 M_\infty + k_6 M_\infty^2)e^{-k_7(M_\infty - k_8)}}{1 + e^{-k_7(M_\infty - k_8)}}, \qquad (16)$$

where k_1, k_2, k_3, k_4, k_5, k_6, k_7 and k_8 are empirical coefficients. Specifically, the term $k_1 + k_2 M_\infty + k_3 M_\infty^2$ can be interpreted as the function of best fit for the supersonic range, whereas the term $k_4 + k_5 M_\infty + k_6 M_\infty^2$ can be interpreted as the function of best fit for the subsonic range. Furthermore, k_7 can be interpreted as the logistic growth rate of the transonic range and k_8 can be interpreted as the mid-range value of the transonic range. By performing a nonlinear least-squares regression in *MatLab*, the function of best-fit for Equation (16) was determined explicitly. Both the data points and the function of best-fit were plotted in the same graph using *MatLab*. The graph is displayed in Figure 18.
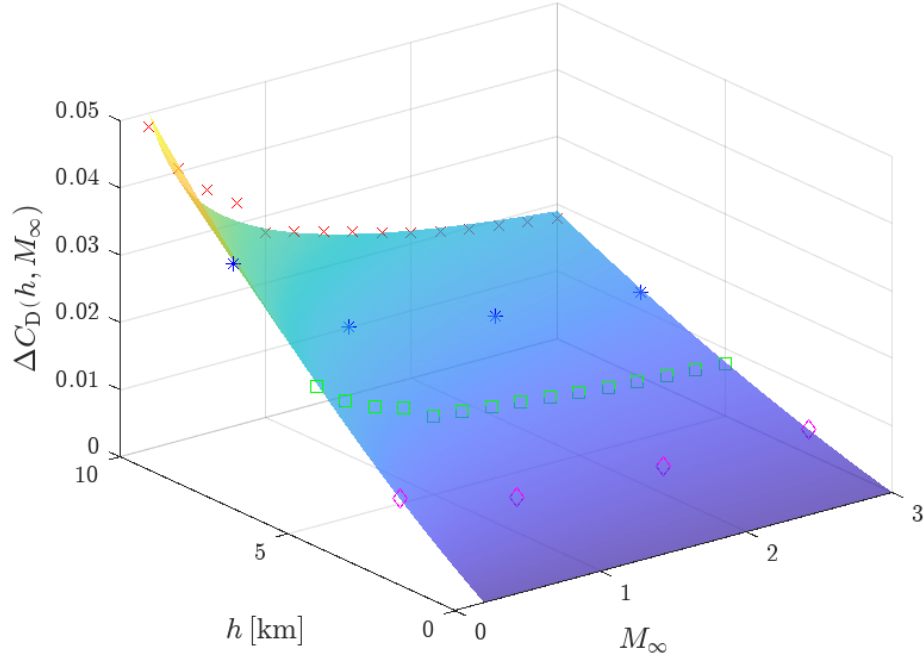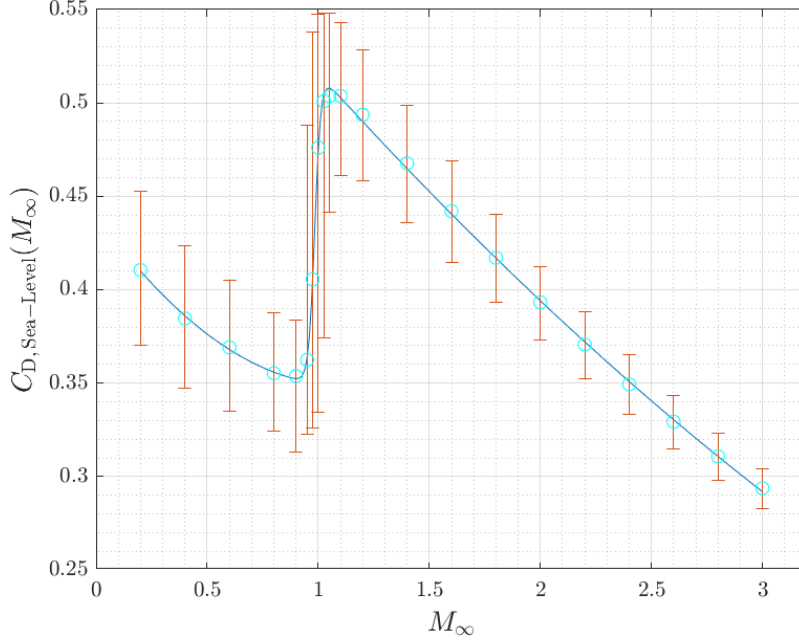
Figure 18: Plot of the regression model for the drag coefficient at sea-level conditions.

The cyan circles in Figure 18 represent the drag coefficients extracted from *Ansys Fluent* at standard sea-level conditions and the line represents the fitted function. Additionally, the red error bars represent the variation of the drag coefficient with an ambient temperature change of $\pm 5\,\%$ (in Kelvins) from standard sea-level conditions. The upper bars represents an ambient temperature of approximately $302\,\mathrm{K}$ and the lower bars represents a temperature of approximately $273\,\mathrm{K}$. The numerical values of the error bars were calculated using the difference between the values in Table 9 and Tables 14 and 15 of Appendix A or linearly interpolated for intermediate freestream Mach numbers. These error bars quantify possible deviations in the drag coefficient due to realistic variations in atmospheric conditions and potential modeling errors in the CFD simulations. It should be noted that the random error in this investigation was exceptionally low and therefore, only possible systematic errors were quantified. Naturally, such systematic error would also likely affect the data points in Figure 17, although these errors were not calculated owing to time considerations.

By inspection, it appears as though the regression model in Figure 18 marginally overpredicts the drag coefficients at $1.0 < M_\infty < 1.1$ and marginally underpredicts the drag coefficients at $1.1 < M_\infty < 1.6$. However, the overall regression statistics indicate an excellent fit, since the root mean square error was found to be 0.00238 and the p-value was $3.87 \cdot 10^{-29}$. Additionally, all model coefficients were determined to be statistically significant, because the maximum coefficient p-value was 0.00313, which is less than the $1\,\%$ threshold used in this investigation to discard the coefficient. It should be noted that this empirical regression model was determined for the *Mjöllnir* rocket using standard sea-level conditions and can be treated as potentially valid for $0.2 \leq M_\infty \leq 3.0$. Exact coefficient values and statistics are given in Table 7. All coefficients in Table 7 are dimensionless.

26

Table 7: Empirical coefficient values for the drag coefficient at sea-level conditions

Coefficient	Estimate	p-value
k_1	0.657	$1.27 \cdot 10^{-19}$
k_2	-0.151	$6.80 \cdot 10^{-11}$
k_3	0.00979	0.000278
k_4	0.440	$1.02 \cdot 10^{-18}$
k_5	-0.164	$8.80 \cdot 10^{-6}$
k_6	0.0740	0.00313
k_7	72.1	$9.47 \cdot 10^{-11}$
k_8	0.985	$3.02 \cdot 10^{-33}$

Thus, Equations (15) and (16) inset into Equation (14) empirically describe the entire dataset of drag coefficients extracted from *Ansys Fluent* for the *Mjöllnir* rocket. This relation can be considered accurate for $h \leq 10\,\mathrm{km}$ and $0.2 \leq M_\infty \leq 3.0$. Through inspection of Figures 17 and 18, combined with the regression statistics presented in this section, it seems fully possible that these empirical models could accurately approximate physical reality, provided their excellent fit with the simulation data.

7 Evaluation

It is important to recognize the validity range of the results in this investigation, as well as the investigation's inherent strengths and limitations. In particular, the assumptions and simplifications made throughout the investigation are emphasized in this section.

7.1 Assumptions and Simplifications

An axisymmetric, simplified rocket geometry subjected to steady-state flow at an angle-of-attack of zero was examined in this investigation. It was assumed that the rocket behaves as a rigid body with no heat transfer between the surrounding air and the rocket body. Additionally, the propulsion system was assumed to be inactive, which implies that the results are not valid for a rocket ejecting propellant from its engine nozzle, since this influences the flow field and thereby the drag coefficients. Moreover, this investigation assumes that there is no significant wall interference and that the incoming air has low turbulence.

7.2 Strengths

One of the major strengths of this investigation was that an empirical model was found that almost perfectly describes how the *Mjöllnir* rocket's drag coefficients varies with the freestream Mach number and altitude, simultaneously. As the freestream Mach number and altitude were the two independent variables in this investigation, this implies that the empirical model describes the full dataset obtained in this investigation with a high degree of precision. Due to the excellent fit of the models to the data, it is possible that the derived empirical models accurately approximate physical reality. Therefore, these models merit further investigation in future research.

Furthermore, the random error could be reduced to insignificant levels in this investigation by running the simulations for sufficiently many iterations until the results had completely converged. Therefore, the results in Tables 9, 10, 11, 12, 13, 14 and 15 of Appendix A can be considered almost exact to numerical precision levels and hence, also the calculated drag coefficients shown in Figures 16, 17 and 18. On the other hand, all potential sources of systematic error were not exhaustively examined, which may impact the results.

7.3 Limitations

It should be noted that the empirical models described by Equations (15) and (16) could potentially be the result of overfitting functions to the simulation data. Specifically, for the altitude correction factor, three model parameters were fitted onto 38 data points in three dimensions, whereas for the drag coefficient at sea-level data, eight model parameters were fitted onto 21 data points in two dimensions. Especially in the latter case, there exists a risk of overfitting. Although this could be partially mitigated by making more observations, the number of observations made in *Ansys Fluent* for the drag force was limited by the computational resources available and the time duration of running each simulation. However, it is also important to consider that the CFD data was exceptionally precise and thus, the function of best fit did not strongly have to account for "noise" in the data, it merely needed to avoid finding unlikely trends. Thus, relatively simple hypotheses were made using elementary functions that seemed to fit the data well. As a rule of

thumb, hypotheses that necessitated coefficients with units to be raised to the power of a non-integer value were avoided. Otherwise, the simplest hypothesis that fitted the data well was chosen.

Likewise, the regression model accuracy was naturally limited by accuracy of the CFD simulations. In particular, it is possible that the results from the CFD simulations deviate from the true values in a systematic manner, due to the stated assumptions and simplifications made in this investigation. Whereas certain sources of systematic error, such as the fluid domain's exterior dimensions, were largely mitigated and other sources were quantified and found not to drastically affect the results, many were left unexamined. Two examples of this are the specific RANS turbulence model employed and the effect that modeling the rocket geometry as a solid capable of heat transfer would have had on the results. However, considering that these are common modeling simplifications/assumptions in CFD, it was assumed that it did not contribute significantly to the systematic error in this investigation

7.4   Explaining OpenRocket Results

The *OpenRocket* software overpredicted the drag coefficient of the *Mjöllnir* rocket for all examined freestream Mach numbers and altitudes. Likewise, there was a clear systematic error when the drag coefficients were calculated in the subsonic range. Hence, it is important to consider why the *OpenRocket* results deviated from the *Ansys Fluent* results. The most likely explanation seems to be that the simplified models used to calculate the drag coefficient in *OpenRocket* do not fully capture the drag coefficient's complex geometric dependencies. For instance, the *Mjöllnir* rocket has a boattail as shown in Figures 7 and 10. However, *OpenRocket* only accounts for the base area reduction associated with boattail, but not the actual changes in flow characteristics associated with directing air into the wake behind the rocket, as detailed in Niskanen (pp. 90). This could partially explain why the results provided in *OpenRocket* were always overestimates, yet why *OpenRocket* predicted a monotonic increase of the drag coefficients in the subsonic range, as shown in Figure 16, remains unaccounted for. Potentially, this could be attributed to certain rockets exhibiting such aerodynamic behavior in the subsonic regime, as indicated in Okninski et al. (pp. 50), and the *OpenRocket* software being specifically calibrated for such rocket geometries. Although both Okninski et al. (pp. 50) and Niskanen (pp. 46-50) seem to rely on Fleeman's empirical formulae (pp. 22) to determine the pressure base drag coefficient of a rocket. Specifically, Fleeman's empirical formulae (pp. 22) require that the pressure base drag coefficient monotonically increases with the Mach number in the subsonic range. As the pressure base drag comprises a major component of the total drag experienced by a rocket, the provided drag coefficient trends in Okninski et al. (pp. 50) and Niskanen (pp. 46-50) are likely dominated by Fleeman's formula (pp. 22) for the pressure base drag coefficient in the subsonic range. However other studies, such as Srivastava et al. (pp. 4) and Sagliano (pp. 3), find that the drag coefficient monotonically decreases in the subsonic range similarly to this investigation. This indicates that Fleeman's formulae (pp. 22) may not apply to all rocket geometries or that the pressure base drag coefficient has a lesser effect on the total drag coefficient than assumed in Okninski et al. (pp. 50) and Niskanen (pp. 46-50). Additionally, according to Hoerner (pp. 6_16), the drag coefficient will, in general, decrease with the Reynolds number for a streamlined body in the low subsonic range. Note that both the Reynolds number and the Mach number are directly proportional to the flow velocity according to Equations (1) and (2) and these numbers are directly proportional to each other for fixed atmospheric conditions. Therefore, it seems that *OpenRocket* is best used only as a rough estimate for drag coefficient of a

rocket and should not be interpreted as exact.

7.5   Potential Applications of Research

This research could be used to improve the drag coefficient calculations for rockets and could also serve as a guideline for important effects to consider when estimating the drag coefficient, such as altitude variation. Additionally, future research could examine if the simulation data in this investigation agrees with experimental results and if the validity range of the model could be extended. Moreover, the empirical drag coefficient model derived in this investigation could be studied for other rocket geometries or aerospace vehicles to determine if the model is generally applicable or if it is only suited for the *Mjöllnir* rocket geometry. Assuming that it is in fact applicable for other rocket geometries, it would be interesting to examine how changes in the rocket geometry influence the empirical coefficients in the drag coefficient model. Similarly, if the empirical model is adjusted to account for an active propulsion system, such as Sabhon et al. (pp. 14-15) and Kim et al. (pp. 7-20) researched, it would be possible to use the model to optimize a rocket's flight speed to minimize fuel consumption and ultimately travel farther with rockets.

8   Conclusion

As shown in this investigation, *OpenRocket* consistently overpredicts the drag force experienced by the *Mjöllnir* rocket for all examined freestream Mach numbers and altitudes. Likewise, it does not account for how the drag coefficient changes with various parameters that influence the drag coefficient, which implies that the predicted drag coefficients should never be interpreted as exact. Instead, an empirical relationship was found for how the *Mjöllnir* rocket's drag coefficient changes with altitude and the freestream Mach number. The empirical relationship fitted exceedingly well with simulation data and merits further investigation. A recommended improvement for estimating the drag coefficients of a rocket would be to collect a database of various rocket's drag coefficients. This could be used to determine how changes in rocket geometry influence the regression model coefficients of an empirical formula. This would likely yield a better approximation of a rocket's drag coefficients, compared to using semi-empirical formulae that often depend on relatively unrealistic and idealized assumptions about the flow behavior. Lastly, the model derived in this investigation could be used to more accurately determine the drag force experienced by rockets and hence, also provide more accurate predictions about rockets' flight trajectories and velocities.

Appendix

Appendix A - Raw Data

The exact data for the drag coefficients calculated in *OpenRocket* is presented in Table 8. Likewise, the computed drag forces in *Ansys Fluent* are shown in Tables 9, 10, 11, 12, 13, 14 and 15 for different freestream Mach numbers, altitudes and ambient temperatures. All data can be considered exact to the last declared significant figure.

Table 8: OpenRocket drag coefficients without fin-induced drag

Freestream Mach Number	Drag Coefficient
0.2	0.520
0.4	0.534
0.6	0.559
0.8	0.592
0.9	0.612
0.95	0.628
0.975	0.638
1.0	0.649
1.025	0.651
1.05	0.655
1.1	0.648
1.2	0.629
1.4	0.590
1.6	0.549
1.8	0.508
2.0	0.472
2.2	0.442
2.4	0.414
2.6	0.390
2.8	0.371
3.0	0.355

Table 9: Ansys Fluent results at sea-level conditions

Freestream Mach Number	Drag Force [N]
0.2	23.4059
0.4	87.7184
0.6	189.4128
0.8	324.146
0.9	408.4454
0.95	466.209
0.975	549.4991
1.0	678.547
1.025	750.1309
1.05	791.4286
1.1	868.8796
1.2	1013.2906
1.4	1306.4985
1.6	1613.0204
1.8	1926.250
2.0	2242.086
2.2	2557.1416
2.4	2867.9707
2.6	3173.2976
2.8	3472.8933
3.0	3767.7935

Table 10: Ansys Fluent results at an altitude of 2.5 km

Freestream Mach Number	Drag Force [N]
0.2	17.6687
1.0	505.738
2.0	1669.667
3.0	2813.0823

Table 11: Ansys Fluent results at an altitude of 5 km

Freestream Mach Number	Drag Force [N]
0.2	13.1077
0.4	48.8869
0.6	105.215
0.8	179.6378
1.0	370.6153
1.2	552.4775
1.4	712.498
1.6	879.931
1.8	1051.016
2.0	1223.644
2.2	1395.898
2.4	1566.2902
2.6	1734.1495
2.8	1899.3527
3.0	2062.0845

Table 12: Ansys Fluent results at an altitude of 7.5 km

Freestream Mach Number	Drag Force [N]
0.2	9.5620
1.0	266.759
2.0	879.516
3.0	1484.7826

Table 13: Ansys Fluent results at an altitude of 10 km

Freestream Mach Number	Drag Force [N]
0.2	6.8459
0.4	25.3975
0.6	54.4652
0.8	92.7812
1.0	187.978
1.2	279.6246
1.4	360.6328
1.6	445.4631
1.8	532.076
2.0	619.5148
2.2	706.798
2.4	793.4894
2.6	879.2241
2.8	963.7161
3.0	1046.7965

Table 14: Ansys Fluent results at sea-level conditions with an ambient temperature of $302\,\mathrm{K}$

Freestream Mach Number	Drag Force [N]
0.2	25.8165
0.8	353.6846
0.9	452.7775
0.95	628.0941
0.975	728.9028
1.0	780.6217
1.025	820.8298
1.05	861.290
1.1	936.9468
1.2	1084.8008
2.0	2352.3572
3.0	3901.1709

Table 15: Ansys Fluent results at sea-level conditions with an ambient temperature of $273\,\mathrm{K}$

Freestream Mach Number	Drag Force [N]
0.2	21.1106
0.8	295.8182
0.9	371.6453
0.95	415.3637
0.975	441.819
1.0	476.5398
1.025	560.3022
1.05	693.9105
1.1	795.537
1.2	940.6882
2.0	2128.5996
3.0	3629.8892

Appendix B - Atmospheric Model

In this investigation, the International Standard Atmosphere (ISA) model of the troposphere was used to model the atmosphere according to ISO 2533:1975 (pp. 1-5). In the ISA model, air at standard sea-level conditions is set according to Table 16.

Table 16: Air at standard sea-level conditions

Property	Symbol	Value	Unit
Pressure	p_{atm}	101.325	kPa
Density	ρ_{atm}	1.225	$\text{kg} \cdot \text{m}^{-3}$
Temperature	T_{atm}	288.15	K
Dynamic viscosity	μ_{d}	$1.789 \cdot 10^{-5}$	$\text{Pa} \cdot \text{s}$
Heat capacity ratio	γ	1.4	-
Specific gas constant	R^*	287	$\text{J} \cdot \text{kg}^{-1} \cdot \text{K}^{-1}$
Gravity of Earth	g	9.807	$\text{m} \cdot \text{s}^{-1}$

Furthermore, Table 17 shows how the ambient temperature in the ISA model of the atmosphere linearly changes with the geopotential altitude.

Table 17: International Standard Atmosphere (ISA) Model of the Troposphere

Layer	Geopotential Altitude [m]	Lapse Rate [K/km]
Troposphere	0	−6.5
Tropopause	11000	0.0

The geopotential altitude is defined as

$$z = \frac{r_0 h}{r_0 + h},\tag{17}$$

where z is the geopotential altitude, r_0 is the approximate radius of Earth and h is the altitude above sea-level. Specifically, r_0 is set to 6356766 m in the ISA model. Using the data in Table 16 as initial values, combined with the ideal gas law and data in Table 17, the differential equation

$$\frac{\mathrm{d}p}{\mathrm{d}z} = -\rho g,\tag{18}$$

can be solved analytically for the ambient atmospheric pressure, p, as a function of the geopotential altitude, z. Additionally, g denotes the gravity of earth and ρ the ambient air density. By insetting Equation (17) into the solved differential equation, the ambient atmospheric pressure as a function of the altitude, h, can be found for the troposphere. The ambient temperature can be found directly using Table 16, Table 17 and Equation (17), whereas the ambient density can be found using the ideal gas law when the ambient pressure and temperature are known.

References

Anderson, D. John. "Flight (Aerodynamics)." *Encyclopedia of Physical Science and Technology*, Third ed., 2003, pp. 1-21. *Elsevier BV*, https://doi.org/10.1016/B0-12-227410-5/00915-7.

ANSYS. "Ansys Fluent Theory Guide." Jul. 2023. PDF.

ANSYS. "Ansys Fluent User's Guide." Jul. 2023. PDF.

Barrowman, James S. "The Practical Calculation of the Aerodynamic Characteristics of Slender Finned Vehicles." 1 Mar. 1967, *The Catholic University of America*, Master's thesis, https://ntrs.nasa.gov/api/citations/20010047838/downloads/20010047838.pdf.
Accessed 1 Jun. 2024.

Benson, Tom. "Real Gas Effects." *NASA*, Glenn Research Center, 7 May 2021, www.grc.nasa.gov/www/BGH/realgas.html. Accessed 29 Apr. 2024.

Çengel, Yunus A., and John M. Cimbala. Fluid Mechanics: Fundamentals and Applications. Third ed., McGraw-Hill, 2014.

Courant, Richard, et al. "On the Partial Difference Equations of Mathematical Physics." *IBM Journal of Research and Development*, vol. 11, no. 2, Mar. 1967, pp. 215-234. *IBM*, https://doi.org/10.1147/rd.112.0215.

Fleeman, Eugene L. Missile Design Guide. AIAA, 2022.

Hammargren, Kristoffer. "Aerodynamics Modeling of Sounding Rockets." 2018, *Luleå University of Technology*, Master's thesis, https://www.diva-portal.org/smash/get/diva2:1241365/FULLTEXT02.pdf.
Accessed 16 Nov. 2023.

Hoerner, Sighard F. Fluid-Dynamic Drag., Hoerner Fluid Dynamics, 1965.

International Organization for Standardization. "International Standard ISO 2533:1975." May. 1975. PDF.

Kim, Yongchan, et al. "Base Flow and Drag Characteristics of a Supersonic Vehicle with Cold and Hot Jet Flows of Nozzles." *Aerospace*, vol. 10, no. 10, 2023, pp. 1-21. *MDPI*, https://doi.org/10.3390/aerospace10100836.

López, Deibi, et al. "Impact of turbulence modelling on external supersonic flow field simulations in rocket aerodynamics." *International Journal of Computational Fluid Dynamics*, vol. 27, no. 8–10, Dec. 2013, pp. 332–341. *Taylor & Francis Online*, https://doi.org/10.1080/10618562.2013.867951.

Mian, Zia, et al. "Early Warning in South Asia - Constraints and Implications." *Science & Global Security*, vol. 11, no. 2-3, Jun. 2010, pp. 109–150. *Taylor & Francis Online*, https://doi.org/10.1080/714041033.

Niskanen, Sampo. "Development of an Open Source Model Rocket Simulation Software." 2009, *Helsinki University of Technology*, Master's thesis, *OpenRocket*, 10 May 2013, https://openrocket.info/documentation.html. Accessed 16 Nov. 2023.

Okninski, Adam, et al. "Development of the Polish small sounding rocket program." *Acta Astronautica*, vol. 108, 2015, pp. 46–56. *Elsevier BV*, https://doi.org/10.1016/j.actaastro.2014.12.001.

Sagliano, Marco. "Apollo 11 Reloaded: Optimization-based Trajectory Reconstruction." *AIAA Journal*, 4 Jan. 2021, pp. 1–17. *Aerospace Research Central*, https://doi.org/10.2514/6.2021-1344.

Sahbon, Nezar, et al. "A CFD study of the aerodynamic characteristics of Twardowsky and FOK rockets." *Transactions on Aerospace Research*, vol. 2022, no. 1, 22 Mar. 2022, pp. 35–58. *Sciendo*, https://doi.org/10.2478/tar-2022-0003.

Srivastava, Nilabh, et al. "Influence of nozzle random side loads on launch vehicle dynamics." *Journal of Applied Physics*, vol. 108, no. 4, 15 Aug. 2010, pp. 1-19. *AIP Publishing*, https://doi.org/10.1063/1.3457887.